RSC Advances

PAPER

View Article Online
View Journal | View Issue

Cite this: *RSC Adv.*, 2023, **13**, 31067

In situ green synthesis of the nanocomposites of MnO_2/graphene as an oxidase mimic for sensitive colorimetric and electrochemical dual-mode biosensing

Yaopeng Liu,[a] Wei Zhao,[bc] Yi Gao,[a] Qing Zhuo,[bc] Tingting Chu,[a] Wensheng Huang,[a] Yin Zheng *[a] and Yingru Li *[bc]

Received 28th August 2023
Accepted 19th October 2023

DOI: 10.1039/d3ra05879d

rsc.li/rsc-advances

Herein we report the colorimetry and an electrochemical for the determination of dopamine (DA) by using MnO_2 nanoparticles and graphene nanosheets composite (MnO_2@G) that display oxidase mimicking property. MnO_2@G could directly oxidize colorless 3,3′,5,5′-tetramethylbenzidine (TMB) into a blue product (oxTMB) without extra oxidants such as H_2O_2. Nevertheless, the presence of DA will inhibit the TMB oxidation due to the presence of the competitive reaction of MnO_2@G and DA, giving a product color change from blue to colorless. A colorimetric assay for detect the concentration of DA was worked out according to this finding. Response is linear in the 0.1 to 15 μM DA concentration range, and the detection limit is 0.14 μM. Wider detection range is achieved in an electrochemical method which is due to the pronounced electrocatalytic activity of MnO_2@G. The MnO_2@G was modified on the surface of the glassy carbon electrode in order to fabricate one type electrochemical sensor. The sensor achieves a wide detection two linear ranges from 0.4 to 70 μM, with the detection limit of 1.16 μM. The detection of DA in real serum sample proved that the nanozyme based on MnO_2@G could be developed into a colorimetry and electrochemical dual-readout sensing platform.

1. Introduction

In spite of highly efficient catalytic ability and excellent selectivity, natural enzymes are associated with many disadvantages, such as high-cost extraction, easy deterioration and poor stability, which restrict their applications.[1] To overcome these shortages, enzyme-mimetic nanomaterials (nanozymes), with low-cost and highly stable substitutes, have been developed and applied in a variety of fields.[2,3] Over the past few years, nanozymes are utilized in many applications, such as sensing, catalysis, imaging, therapeutics, pollutant removal and beyond.[2,4–6] Especially in the sensing field, nanozymes have been found intensively useful for biochemical detection, environmental monitoring and food analysis.[7–9] Xu *et al.* reported a KCl-doped lignin carbon dots nanozymes with peroxidase-like activity and applied the nanomaterial for colorimetric detection of glutathione.[10] Ren *et al.* designed a tunable structure defect strategy to regulate the nanozyme activity of MOFs for the online electrochemical detection of uric acid.[11] Ge *et al.* developed a colorimetric assay for quantitative malathion detection based on the oxidase-mimicking activity of Fe–N/C SAzymes, and the detection technology was successfully applied in environmental and food samples.[12] Han *et al.* recently designed 2D Fe–Mn bimetallic nanozyme (Dex-FeMnzyme) with highly oxidase-like activity for the total antioxidant capacity (TAC) assay, Dex-FeMnzyme showed satisfactory sensitivity and convenient colorimetric biosensor TAC.[13] Nowadays, although colorimetric or electrochemical sensors based on nanozyme have been used to detect different analytes, there are still some shortcomings for some nanozymes, such as low catalytic activity, poor stability or single form of detection.[14,15] Dual-mode detection methods gradually becomes a new focus, because they not only provide more than one signal output mode, but also offer good accuracy and diversified results.[16,17] Therefore, there is an urgent need to prepare a multifunctional nanozyme with both intrinsic enzyme-like catalytic activity and electrocatalytic activity, and use it to construct a dual-mode sensing platform for colorimetric and electrochemical sensors.

Currently, it is reported that nanozymes are broadly classified according to the composition of nanomaterials, including precious metals (gold, silver, platinum, palladium, *etc.*), metal oxides and sulfides (MnO_2, CeO_2, MoS_2, VS_2, *etc.*), carbon-based nanomaterials (fullerenes, carbon nanotubes, carbon nanodots,

[a]*College of Chemical and Environmental Engineering, Hubei Minzu University, Enshi 445000, Hubei, China. E-mail: zhengyin0617@163.com*

[b]*College of Intelligent Systems Science and Engineering, Hubei Minzu University, Enshi, 445000, China. E-mail: Liyingru@outlook.com*

[c]*Key Laboratory of Green Manufacturing of Super-light Elastomer Materials of State Ethnic Affairs Commission, Hubei Minzu University, Enshi, 445000, China*

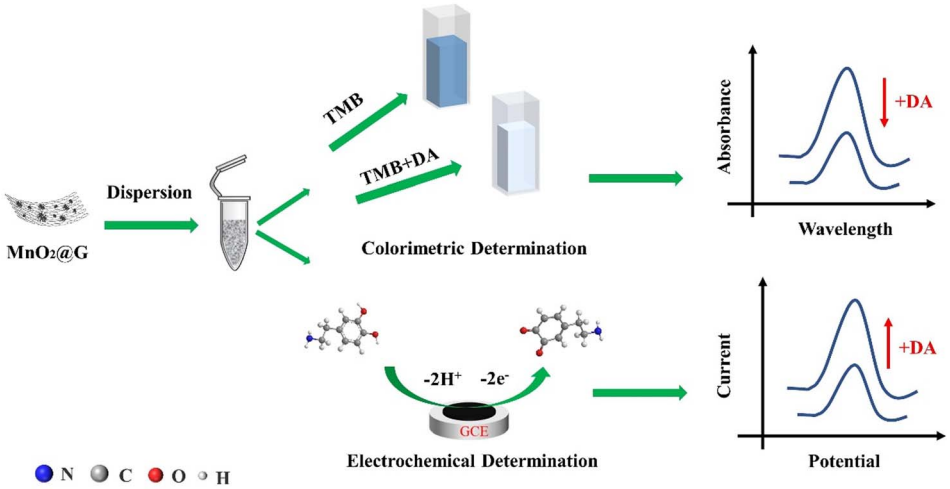

Scheme 1 Colorimetric and electrochemical assay for DA.

graphene, *etc.*), metal–organic frameworks (MOFs) and their derivatives, *etc.*[1,18–25] Among these nanozymes, graphene materials/composites are attracting increasing attention because of their excellent electron transfer capability and synergistic effect.[26–28] Numerous graphene-based nanozymes have been developed and mainly depend on the following two strategies. The first one is functionalizing graphene, in which graphene materials are modified with functional groups to improve catalytic activity. For example, Song *et al.* prepared carboxyl-modified graphene oxide with peroxidase-like activity by covalently grafting polyethylene glycol onto the graphene oxide of chemically activated surfaces and edges.[29] Liu *et al.* recently reported a kind of peroxidase-like nanozymes, prepared by reducing and functionalizing graphene oxide by Ganoderma polysaccharide.[30] The other one is preparing graphene-based composites, in which their enzyme-mimetic activity can be further enhanced. For instance, Guo *et al.* have developed a nanozyme of peroxidase-like activity by depositing PtCu bimetallic nanoparticle on polystyrene-sulfonate-functionalized graphene.[31] Wang *et al.* prepared a composite with oxidase-like activity consisting of $NiCo_2S_4$ and reduced graphene oxide (rGO) *via* a hydrothermal process.[32] Song *et al.* demonstrated that fluoride capped V_6O_{13}-rGO nanocomposites exhibited high oxidase mimetic activity for the first time.[33] Nevertheless, most of these nanozymes may still encounter with some problems like low catalysis activity, complicate synthesis and high cost, hindering their further application. Therefore, it is of great interest to develop new graphene-based nanozymes with easy preparation, high catalytic activity and low cost. Although it has been reported that graphene-based composites are used for sensing different analytes, their material synthesis steps are complicated.[34] In addition, there are few studies on the simultaneous use of MnO_2@G composites with nanozymes activity for the construction of colorimetric and electrochemical sensors.

In this work, an *in situ* green synthesis method is proposed, and a novel composite constructed by MnO_2 nanoparticles and graphene nanosheets (MnO_2@G) is prepared *via* a modified Hummers' method and the following after-treatment. In detail, the impurities of Mn^{2+} ions in crude graphene dispersion are oxidized by additional MnO_4^- to *in situ* generate MnO_2 nanoparticles on or between graphene sheets. Therefore, the MnO_2@G were obtained facilely and economically. Moreover, a novel colorimetric and electrochemical dual-channel sensor for the determination of dopamine (DA) is developed by utilizing MnO_2@G as an oxidase mimic. MnO_2@G can directly catalyze 3,3′,5,5′-tetramethylbenzidine (TMB) to convert colorless TMB to blue oxidized production (oxTMB), showing a superior oxidase activity. Under the optimized conditions, the concentration of DA was quantitatively determined by the UV-vis absorbance (652 nm) of oxidized TMB. Meanwhile, it is noted that MnO_2@G modified electrodes possess excellent electrocatalytic activity to the oxidation of DA. The MnO_2@G-based electrochemical sensor shows a wider detection range toward DA. Moreover, the colorimetric and electrochemical dual-mode sensor based on MnO_2@G was constructed for the detection of DA with limit of detection (LOD) of 0.14 μmol L^{-1} and 1.16 μmol L^{-1}, respectively (Scheme 1).

2. Experimental section

2.1 Materials and instruments

Graphite powders (325 mesh), dopamine (DA), 3,3′,5,5′-tetramethylbenzidine (TMB), L-glycine (Gly) and other amino acid was purchased from Shanghai Aladdin Bio-Chem Technology Co., Ltd (Shanghai, China); the potassium permanganate ($KMnO_4$), sulfuric acid (purity: 98%, H_2SO_4), potassium hydroxide (KOH), ethanol, *N*,*N*-dimethylformamide (DMF), hydrogen peroxide (purity: 30%, H_2O_2) and other reagents were obtained from Sinopharm Chemical Reagent Co., Ltd (Shanghai, China); the concentrations of KH_2PO_4–Na_2HPO_4 and CH_3COOH–CH_3COONa were 0.1 M and 0.2 M, respectively, for the preparation of a PBS and NaAc-Hac buffer solution. The ultrapure water was used as experimental water throughout the experiment.

UV-vis spectra were performed by a Shimadzu UV-2550 UV Visible spectrophotometer (Shimadzu Co., Kyoto, Japan).

Electrochemical experiments were performed using a CHI-660E electrochemical workstation (Chenhua Apparatus Co., Shanghai, China). The scanning electron microscopy (SEM) images were obtained using a scanning electron microscope (Quanta FEG 250 FEI, USA). Transmission electron microscopy (FEI Tecnai F20, FEI, USA) was used to record the high-resolution TEM images. The crystal structures of the samples were characterized by X-ray diffraction (XRD-7000, Shimadzu, Japan). X-Ray Photoelectron Spectroscopy (XPS) was recorded by Kratos AXIS Supra spectrometer (Ultima IV, Rigaku Corporation, Japan).

2.2 Synthesis of MnO_2@G

The graphene was prepared from graphite powder using an improved Hummers' method.[35,36] Firstly, 5 g graphite powder was put into 150 mL H_2SO_4, and then 15 g $KMnO_4$ was added to the reaction system under ice condition slowly, followed by stirring for 0.5 h. Successively, the reaction system was transferred to a 40 °C water bath and stirred for about 1 h. After that, 500 mL H_2O and sufficient H_2O_2 were added to turn the color of the solution from dark brown to yellow. Then, KOH was slowly added into the solution and turned the pH of the solution to 7 ± 1 with agitation. Finally, 10 g $KMnO_4$ were added again and sufficiently stirred for 4 h at 85 °C to proceed comproportionation reaction of Mn element. The obtained products were filtrated and then washed with H_2O. After drying under 80 °C and successively thermal treatment under 120 °C to reduce graphene MnO_2@G was obtained.

2.3 Fabrication of the enzymatic-like modified electrode

The glassy carbon electrode (GCE) was polished on a polishing cloth with 0.05 μm alumina slurry, successively ultrasonically cleaned in ethanol and ultra-pure water respectively and then dried in room temperature before use. The MnO_2@G modified GCE (named MnO_2@G/GCE) was fabricated by dispersing the MnO_2@G in DMF (10 mg mL^{-1}) and drop casting 3 μL of this solution on the GCE surface followed by drying at infrared lamp for 15 minutes.

2.4 Oxidase-like activity of MnO_2@G

By examining the relative catalytic activity (defined as the ratio of the absorbance at the target point to the maximum absorbance) of the MnO_2@G at various temperatures (10–60 °C), pH (3.0–8.0), and response time (1–60 minutes), the optimum reaction conditions for the colorimetric system were found. To assess the oxidase-like activity of MnO_2@G, TMB was chosen as the chromogenic substrate. Typically, MnO_2@G (1.0 mg mL^{-1}, 15 μL) and the TMB (10 mM, 35 μL) were added to NaAc-HAc buffer solutions (0.2 M, pH = 5.0, 2.95 mL). The UV-vis spectrum of TMB + MnO_2@G system was obtained after reaction at 30 °C for 30 minutes.

2.5 Steady-state kinetic study for oxidase-like

To determine the affinity between the MnO_2@G and substrate, steady-state kinetic experiments were implemented under the optimum reaction conditions by altering the TMB concentrations in the TMB + MnO_2@G system. Generally, a series of substrate concentrations of TMB (35 μL) were added into NaAc-HAc buffer solutions (2.95 mL, 0.2 M, pH = 5.0) containing MnO_2@G (15 μL, 1.0 mg mL^{-1}). On a UV-vis spectrophotometer, kinetic tests were conducted in time course mode to record the change in absorbance at 652 nm. According to the Michaelis–Menten equation,[37] $v = V_{max}[S]/(K_m + [S])$, where is the beginning velocity, $[S]$ is the substrate concentration, V_{max} is the maximum velocity, and K_m is the Michaelis constant, the kinetic constants were computed.

2.6 Catalytic mechanism for oxidase-like activity

To investigate the possible reason for the oxidase-like activity of MnO_2@G, TMB catalytic oxidization on O_2-dependent experiments were performed by the nitrogen injected the solution and keeping it for 30 minutes. In addition, in order to explore the reactive oxygen species (ROS) in TMB + MnO_2@G system, some radical scavengers were used. For example, iso-propyl alcohol (IPA, $^{\bullet}OH$ scavenger), sodium azide (NaN_3, $^1O_2$ scavenger) and *p*-benzoquinone (PBQ, $O_2^{\bullet-}$ scavenger) were added respectively to the TMB + MnO_2@G system. The concentrations of IPA, NaN_3 and PBQ were 0.5 mM, 1.0 mM and 2.0 mM.

2.7 Dual-mode sensing platform for DA detection

For DA detection, 50 μL of DA with different concentration, 35 μL of TMB (10 mM), and 15 μL of MnO_2@G (1.0 mg mL^{-1}) were added to NaAc-HAc buffer solutions (2.9 mL, 2.0 M, pH = 5.0). After 30 minutes of incubation at 30 °C, the UV-vis spectrum of TMB + DA + MnO_2@G system at 652 nm was recorded. The linear relationship between the absorbance change value ΔA ($\Delta A = A_0 - A$, A_0 is the absorbance of the blank solution, and A is the absorbance of DA sample solution) and the DA concentration was investigated.

The concentration of DA in a phosphate-buffered solution (PBS, 0.1 M, pH = 5.5) was determined by differential pulse voltammetry (DPV). All electrochemical detections were done in a typical three-electrode setup at room temperature to use a bare GCE or MnO_2@G/GCE as working electrodes, a platinum electrode as the counter electrode, and a calomel electrode as the reference electrode.

2.8 DA assay in human serum samples

The serum was collected from a group of volunteers from the Affiliated Hospital of Hubei Minzu University. The standard additive method was used to show the practical applicability. After diluting the serum with ultra-pure water to a final dilution of 100 times, the serum sample was added with DA standard solution at varying concentrations. Then, DA was detected with the same procedures described above.

3. Results and discussion

3.1 Characterizations of MnO_2@G

The morphologies of the MnO_2@G were examined through scanning electron microscope (SEM). In Fig. 1a shows the

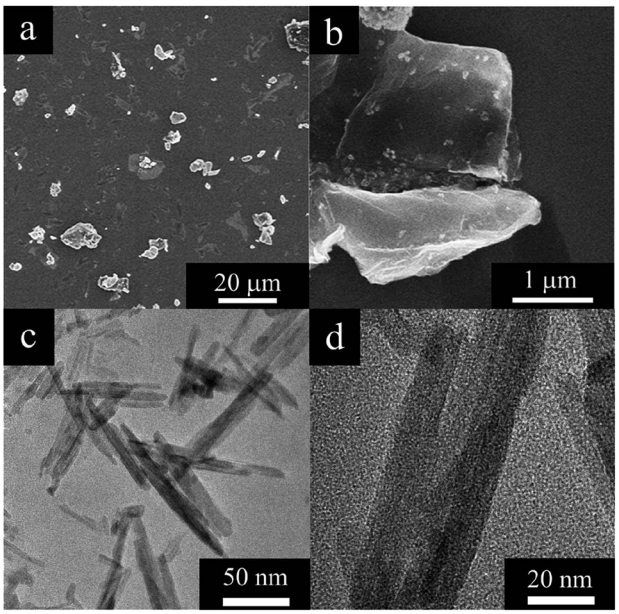

Fig. 1 SEM (a and b) and TEM (c and d) images of a MnO_2@G.

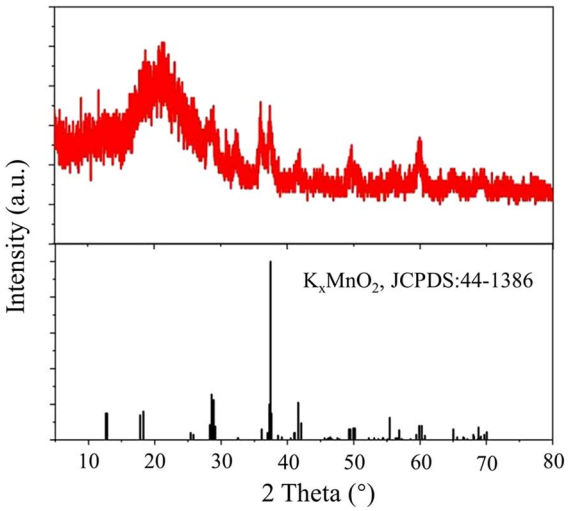

Fig. 2 XRD patterns of MnO_2@G.

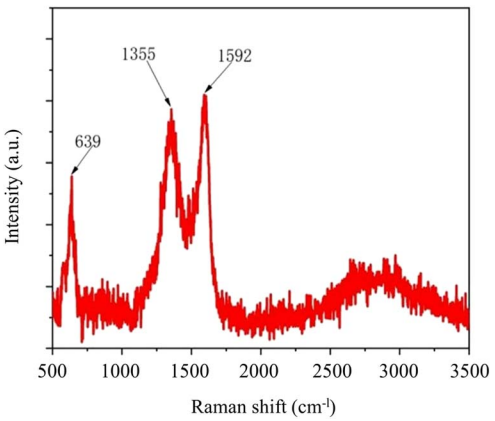

Fig. 3 Raman spectra of MnO_2@G.

irregular sheets structure of MnO_2@G nanocomposite. It is noticed from SEM images with higher magnification (Fig. 1b) that MnO_2 nanoparticles of particle size of ~10 μm was unevenness distributed on graphene sheets. This result showed that both MnO_2 nanoparticles and graphene lamellae did not show agglomeration, MnO_2 nanoparticles distribution were dis-uniformly deposited on the graphene surface. Additionally, the image from TEM depicts showed that the MnO_2 in the shape of nanosized fibrous morphology and some were intertwined nonuniformly on the graphene surface (Fig. 1c and d). The morphology implies that MnO_2 nanoparticles and graphene sheets should have favorable interaction, which would benefit their synergistic effect, and ensure the application of two-mold detection.

The chemical structure of the MnO_2@G was examined by XRD to determine the crystal form of MnO_2. The XRD patterns of the MnO_2@G contain two groups of feature diffraction peaks (Fig. 2): the broad feature diffraction peak at 26° is assigned to lattice plane of graphene (002), which implies that the graphene sheets are exfoliated. Furthermore, five sharp diffraction peaks appeared at 28.6°, 36°, 37.4°, 41.7°, 49.7° and 59.9° are the other group, corresponding to (301), (400), (211), (204), (411) and (512) of facts of K_xMnO_2 (JCPDS no. 44-1386), respectively, demonstrating the fine formation of the cryptomelane-type MnO_2 (K_xMnO_2, where x is non-stoichiometric, around 0.12) crystalline structure of MnO_2, which agrees the formation of K_xMnO_2 crystal observed in TEM. The XRD results proves the success deposition of K_xMnO_2 on graphene surface.

Raman spectrum further confirm the chemical formation of MnO_2@G. Raman spectrum of the material in Fig. 3 clearly show two characteristic peaks of MnO_2@G, D peak (1355 cm^{-1}) and G peak (1592 cm^{-1}) attributing to the presence of defects and the graphite-derived sp^2 carbon structure, which proves the presence of graphene sheets.[30,35,38] Another Raman band at 639 cm^{-1} is the characteristic band of K_xMnO_2.[36,39] According to the ref. 40, the sharp Raman bands at 639 cm^{-1} is the indicative of a tetragonal structure with an interstitial space consisting of (2 × 2) tunnels, due to the symmetric Mn–O vibrations and assigned to the Ag spectroscopic species.

To confirm the formation of MnO_2@G, XPS data of the material were recorded (Fig. 4a). As presented in Fig. 4a, the survey XPS spectrum exhibits the presence of Mn, K, C and O elements in the MnO_2@G with the atomic percentage of 9.4, 0.9, 60.9 and 28.8%, respectively. As shown in Fig. 4b, the peaks of O 1s at 529, 530.6 and 532.5 eV can be respectively attributed to Mn–O–Mn, C=O and C–OH.[41,42] In detail, the C 1s peak can be deconvoluted into three components, with binding energies at 284, 285.3 and 287.6 eV (Fig. 4c), which are ascribed to the graphitic carbons, C–O bonds and C=O bonds. Moreover, the two peaks at 291.1 eV and 293.8 eV were considered as the characteristic peak of K 2p.[43] The high-resolution Mn 2p spectra in Fig. 4d for all samples show the same composition of peaks, including two peaks at 652.9 eV and 641.4 eV, corresponding to the Mn $2p_{1/2}$ and Mn $2p_{3/2}$, respectively. The energy separation

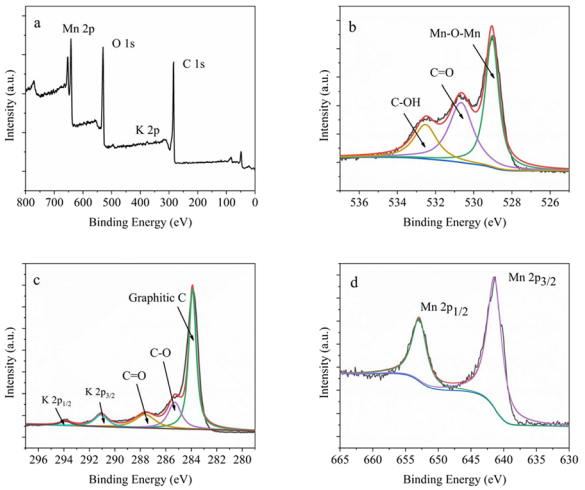

Fig. 4 (a) XPS assay of MnO_2@G; the high-resolution XPS pattern of (b) O 1s, (c) C 1s + K 2p and (d) Mn 2p.

of these peaks was found to be 11.5 eV, which indicates the presence of Mn^{4+} in MnO_2.[44] The above result verified successfully *in situ* formation of MnO_2 on the graphene surface. In summary, in the nanocomposite of MnO_2 and graphene, the cryptomelane-type MnO_2 (K_xMnO_2) provides the metal active site and graphene enhances the electrochemical performance of the materials, which lays the foundation for the subsequent construction of the dual-mode colorimetric-electrochemical sensors.

3.2 Electrochemical investigation of MnO_2@G

Electrochemical impedance spectroscopy (EIS) and cyclic voltammetry (CV) were employed to examine the electrocatalytic characteristics of modified electrodes. The Nyquist curves of the GCE and MnO_2@G/GCE electrodes were shown in Fig. 5a. The diameter of the semicircle at high frequency relates to the electron transfer resistance, whereas the straight portion corresponds to the diffusion process.[45] As seen in Fig. 5a, a large diameter of the semicircle part was observed in the case of GCE. While on the MnO_2@G/GCE has a nearly straight line appeared with the electron transfer resistance value close to zero. This indicates that the electron transfer of $Fe[(CN)_6]^{3-/4-}$ on the surface of MnO_2@G/GCE electrode is faster due to the good electron pathway provided by graphene, which improves the electron transfer efficiency to enhance the conductivity of bare GCE electrode. Besides, the slope of the MnO_2@G/GCE electrode in the low-frequency region is larger than that of the MnO_2@G/GCE electrode, which further indicates that the MnO_2@G can effectively reduce the interfacial resistance and can improve the conducting characteristics of the electrochemical sensor.[46]

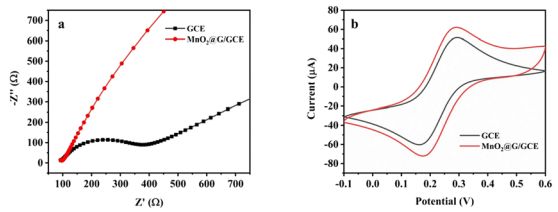

Fig. 5 EIS diagram (a) and CV curves (b) of the various electrodes in 0.1 M KCl solution containing 5 mM $Fe[(CN)_6]^{3-/4-}$.

As illustrated in Fig. 5b, GCE and MnO_2@G/GCE was characterized by CV methods. It can be seen from the figure that a pair of symmetric redox peaks were presented on each electrode, which show a quasi-reversible electrochemical process. The intensity of the redox peak corresponding to MnO_2@G/GCE was substantially greater than that of GCE. The anodic peak current (I_{pa}) on MnO_2@G/GCE were 1.07 times higher than that of CCE, and the cathodic peak current (I_{pc}) on MnO_2@G/GCE were 1.15 times higher than that of CCE. The results of CV indicated that MnO_2@G enhanced electro-catalytic activity and conductivity of the CCE electrode.

3.3 Kinetic analysis of MnO_2@G as an oxidase mimic

To determine the oxidase-like activity of MnO_2@G, the kinetic research was done under the following conditions: 5.0 μg mL^{-1} of MnO_2@G, pH = 5.0 and 30 °C. As shown in Fig. 6a, the typical Michaelis–Menten curves was obtained by changing the concentration of substrate (TMB).[12] The double-reciprocal Lineweaver Burk plots (Fig. 6b) was used to obtain the kinetic parameters Michaelis–Menten constant (K_m) and maximum initial rate (V_{max}), and they are 0.026 mM and 2.52×10^{-8} M s^{-1}, respectively. The kinetic parameters reported in other references and this study were given in Table 1. The K_m represents the affinity between nanozymes and substrate, which the lower value of K_m means a stronger affinity.[47] The results indicated that the value of K_m of MnO_2@G toward TMB lower than that of other oxidase-like nanozymes, indicating a stronger affinity between MnO_2@G and substrates.

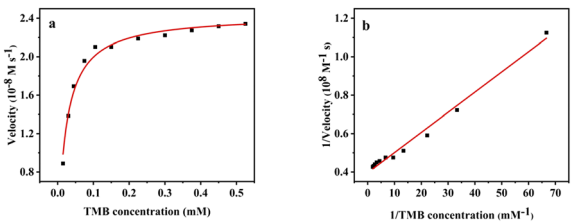

Fig. 6 Steady-state kinetics assays of MnO_2@G by varying concentrations of TMB (a) and corresponding Lineweaver–Burk plots (b).

Table 1 Comparison of kinetic constants of MnO_2@G with different nanozymes

Nanozymes	K_m (mM)	V_m (10^{-8} M s^{-1})	Ref.
MnO_2@G	0.026	2.52	This work
MnO_2/PS	0.068	8.9	48
PtNPs@MnO_2	0.095	26	49
Ag/His-GQD	0.6	22.5	50
V_6O_{13}-rGO + F^-	0.082	4.34	33
HPR	0.53	14.5	51
Laccase	0.19	4.5	52

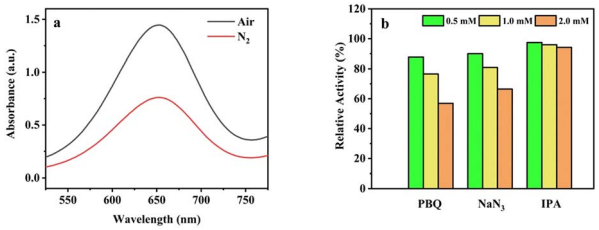

Fig. 7 (a) UV-vis spectrum of TMB + MnO_2@G system in N_2 saturated system. (b) The relative activity of MnO_2@G with different radical scavenger (PBQ, NaN_3 and IPA).

3.4 Investigation of the catalysis mechanism of MnO_2@G

The catalytic mechanism of the oxidase-mimicking activity may originate from the dissolved oxygen to convert reactive oxygen species (ROS), which the oxidize the substrate (TMB).[37] To reveal the role of dissolved oxygen in the oxidation of TMB, a comparative experiment was conducted under a N_2-rich atmosphere. It can be seen from Fig. 7a that the absorbance was decreased by 47.3% when N_2-rich coexist, which proved the important role of dissolved oxygen in the catalytic process and further verify the oxidase-like activity of MnO_2@G.

As shown in Fig. 7b different radical scavengers were used in order to further explore active species in TMB + MnO_2@G system. To determine the ROS coexist, some scavengers, such as *p*-benzo- quinone (PBQ), NaN_3 and iso-propyl alcohol (IPA) were added into the catalytic systems to capture $O_2^{\bullet-}$, $^1O_2$ and $^{\bullet}OH$ reactive oxygen species. As can be seen from Fig. 7b, PBQ ($O_2^{\bullet-}$ scavenger) and NaN_3 ($^1O_2$ scavenger) induces a significant decline in catalytic activity of MnO_2@G, which indicates the existence of $O_2^{\bullet-}$ and $^1O_2$ in this system. The IPA as scavenger of $^{\bullet}OH$ radical has minor effect on the catalytic activity of MnO_2@G. It is indicated that the $O_2^{\bullet-}$ and $^1O_2$ play an important role in the catalytic oxidation of TMB by MnO_2@G.

3.5 Feasibility for colorimetry and electrochemical dual-mode sensing platform

The oxidase activity of MnO_2@G was investigated by conducting a catalyzed reaction with TMB, which resulted in a substantial color shift from colorless to blue. Fig. 8b reveals that MnO_2@G can effectively oxidize TMB to enhance absorbance, with the greatest absorption peak occurring at 652 nm in the MnO_2@G + TMB system. The findings confirmed that TMB oxidation was caused by MnO_2@G decomposing dissolved oxygen. Interestingly, when 10 μM DA was added to the TMB + MnO_2@G system, its blue immediately faded and its absorbance reduced considerably. This behavior may be explained by the inhibition of the catalytic oxidation of TMB by of DA. The above investigation results showed that MnO_2@G can be used as nanozyme for colorimetric analysis of DA.

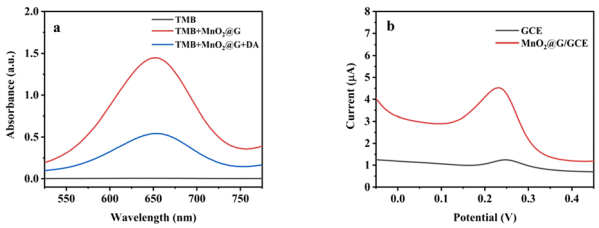

Fig. 8 (a) UV-vis absorption spectra of in different systems in NaAc-HAc buffer (0.2 M pH = 5.0) at 30 °C for 30 min. (b) DPV curves of GCE and MnO_2@G/GCE in PBS (0.1 M pH = 5.5) containing 10 μM DA.

As shown in Fig. 8b, the DPV was used to study the electrochemical behavior of DA on GCE and MnO_2@G/GCE electrodes. The larger peak currents were obvious on the MnO_2@G/GCE than that of GCE. The peak currents on MnO_2@G/GCE were 7.13 times higher than that of CCE. It indicated that the capability of the MnO_2@G/GCE electrode to detect DA is greatly enhanced owing to the capacity of MnO_2@G to enhance the conductivity of the GCE, hence facilitating electron transfer. Therefore, the MnO_2@G modified electrode can be used as an electrochemical analysis platform for DA.

3.6 Condition optimization for the dual-mode sensing platform

For the purpose of more sensitive assay of the dual-mode sensing platform, several parameters in the detection system were optimized. Like natural oxidase, the oxidase-like catalytic activity of MnO_2@G is depends on the pH (Fig. 9a), temperature (Fig. 9b), concentrations of catalyst (Fig. 9c) and reaction time (Fig. 9d). As shown in Fig. 9a, the relative activity of MnO_2@G reached the maximum when the pH of the NaAc-HAc buffer solution was 5.0. Fig. 9b shows that the optimum catalytic temperature of MnO_2@G catalyst is 30 °C. As shown in Fig. 9c with the increase of MnO_2@G concentration, the relative activity of the catalyst gradually increased. However, the rate of increase of relative activity was slow when the concentration of MnO_2@G reached 5 μg mL^{-1}. As shown in Fig. 9d, the relative activity stabilized when the reaction time reached 30 minutes. In summary, the relative catalytic activity of MnO_2@G was most suitable at pH = 5.0, temperature of 30 °C, reaction time of 30 minutes and catalyst concentration of 5 μg mL^{-1}.

To increase the sensitivity of the electrochemical sensor, DPV evaluated the effect of pH on the response current of the sensor. With 30 μM DA as the analyte, MnO_2@G/GCE as the working electrode, and 0.1 M PBS as the supporting electrolyte, the pH was optimized by the peak current response value of DPV. The detection outcome was depicted in Fig. 9e. The current value of DA reaches its maximum when the pH = 5.5. Consequently, the PBS with pH = 5.5 was utilized as the supporting electrolyte in subsequent analyses of the DA. As seen in Fig. 9f, as pH increased, the peak potentials of DA moved in a negative direction, showing that protons were involved in the electrochemical process.[53] Simultaneously, the correlation between peak potential (E_p) and pH was also investigated. According to Fig. 9f, the relationship between peak potential and pH is linear. The equation for linear regression was E_p (V) = −0.054 pH + 0.548 (R^2 = 0.997). The slope is −0.054, which is near to the Nernst value (−0.059),

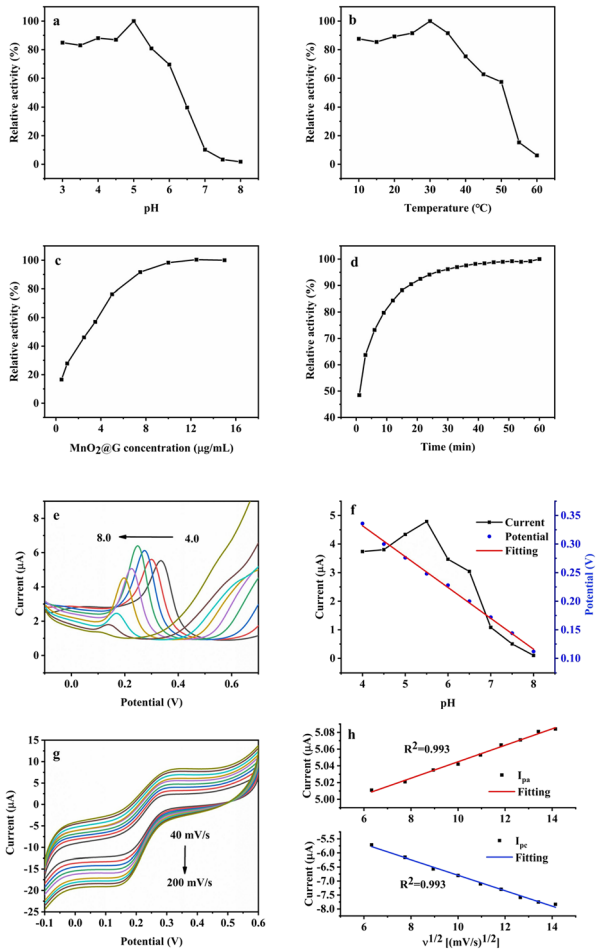

Fig. 9 Dependency of the MnO_2@G catalytic activity on (a) pH values, (b) temperature, (c) the catalyst concentration, and (d) interaction time. DPV curve (e), effect of pH on peak current (f) and linear fitting curve of peak potential and pH (f) of MnO_2@G/GCE in PBS containing 30 μM DA with different pH (pH = 4–8); (g) CV plots of DA with various scan rates from 40 to 200 mV s^{-1} on MnO_2@G/GCE; (h) the linear relationship between peak current and scan rate.

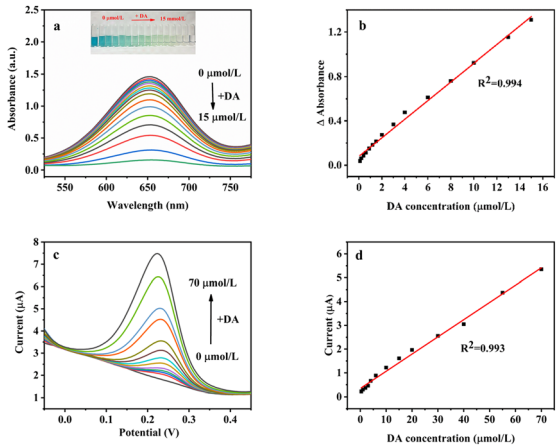

Fig. 10 (a) UV-vis absorption spectra of MnO_2@G combined with different DA concentrations (from top to down DA concentrations are: 0, 0.1, 0.2, 0.4, 0.6, 0.9, 1.2, 1.5, 2, 3, 4, 6, 8, 10, 13, 15 μM). The inset shows the corresponding images. (b) The plotted linear relationships between ΔA and the corresponding [DA]. (c) DPV curves of MnO_2@G/GCE in pH = 5.5 buffer containing different concentrations of DA (0, 0.4, 1, 2, 3, 4, 6, 10, 15, 20, 30, 40, 55, 70 μM). (d) Represent the calibration plot between peak current and DA concentration.

suggesting that the redox process at the MnO_2@G/GCE electrode involves an equal quantity of protons and electrons.[54,55] Using CV method, the impact of different scan rate on MnO_2@G/GCE was recorded. Fig. 9g demonstrates that when the scan rate increased, both the I_{pa} and I_{pc} of DA linearly grew. As shown in Fig. 9g, the two peak currents are proportional to square root of scan rate with a linear regression equation as $I_{pa} = 0.0098\nu^{1/2} + 4.947$ ($R^2 = 0.993$) and $I_{pc} = -0.277\nu^{1/2} - 4.028$ ($R^2 = 0.993$). It is indicated that the electrochemical reaction of DA on MnO_2@G/GCE is a diffusion control process.[56]

3.7 Colorimetric and electrochemical detection of DA

Inspired by the oxidase-like activity of the MnO_2@G, we used TMB + DA + MnO_2@G system for sensitive colorimetric detection of DA. Under the optimal reaction conditions, the absorbance of the system was measured with DA concentration changing from 0.1 to 15 μM as shown in Fig. 10a. A linear curve of ΔA (Δ absorbance is the difference of the absorbance of the solution with and without DA) to DA concentration was shown in Fig. 10b. The results showed that the absorbance decreased with the DA concentration in the range 0.1–15 μM and the calibration equation was $\Delta A = 0.084[DA] + 0.08$ ($R^2 = 0.994$) with the LOD of 0.14 μM (S/N = 3).

To farther broaden the application of MnO_2@G, the DPV method was used to analyze the relationship between concentration and the current response of DA under optimal conditions. The standard curves of the relationship between concentration and current response are shown in Fig. 10c and d. It can be seen from Fig. 10c, as the DA concentration increases from 0.4 to 70 μM, the peak current linear increases. The corresponding linear equation are $I_{pa} = 0.072[DA] + 0.34$ ($R^2 = 0.993$) (Fig. 10d) with the LOD of 1.16 μM (S/N = 3). Compared with these references as listed in Table 2, the proposed two method exhibits a relatively low LOD and wide detection range, confirming the superiority of the proposed complementary-dual-modal sensing platform for DA detection.

3.8 Interferences, stability, and reproducibility

Selectivity is important for the colorimetric sensor for DA based on MnO_2@G. Under optimal conditions containing 10 μM DA, 50-fold inorganic ions such as Na^+, Mg^+, Ca^{2+}, K^+, SO_4^{2-}, Cl^- and 5-fold biomolecules such as Gly, Leu, Lys, Arg, glucose and fructose as several potential interfering substances, signal changes below 5% in absorbance were observed in Fig. 10a. These results demonstrate that the present MnO_2@G based assay shows excellent specificity for DA. MnO_2@G has a stable oxidase-like activity and maintains 96.6% relative catalytic activity when stored at room temperature for 30 days.

The interference of coexisting species on experimental results was investigated. As shown in Fig. 10b, the results show

Table 2 Comparison of analytical performances of different DA assays

Methods	Materials	Linear range (μM)	Detection limit (μM)	Ref
UV-vis	MnO_2@G	0.1–15	0.14	This work
Electrochemistry		0.4–70	1.16	This work
UV-vis	h-CuS NCs	2–150	1.67	57
UV-vis	$NiCo_2S_4$-rGO	0.5–100	0.43	32
UV-vis	Pt/hBNNSs	2–55	0.76	58
Electrochemistry	Pd-NCd/rGo	20–220	7.02	59
Electrochemistry	GO/Fe_3O_4	1–10	0.48	60
Electrochemistry	PtNP/rGO	1–10; 10–100	1.405	61

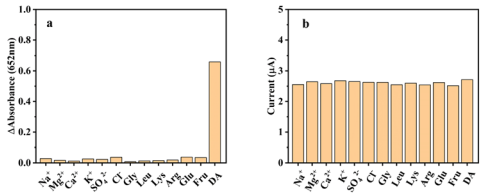

Fig. 11 Selectivity of (a) the colorimetric sensor and (b) the electrochemical sensor.

that 100-fold of inorganic ions such as Ca^{2+}, Na^{+}, K^{+}, Mg^{2+}, SO_4^{2-}, Cl^{-} and 10-fold biomolecules, such as Gly, Leu, Lys, Arg, glucose and fructose do not affect the test results (with signal change below 5% on the height of the peak current). It shows that the electrochemical sensor has sound interferences. Under the optimal experimental conditions, with MnO_2@G/GCE as the working electrode, 30 μM DA is tested in PBS buffer with pH = 5.5 for DPV. The current value changes were observed to verify the stability and reproducibility of the electrode. Using the same MnO_2@G/GCE electrode to scan 15 times under the above conditions, the relative standard deviation (RSD) was 2.4%. MnO_2@G/GCE electrode was placed at room temperature for 7 days. The response current of DA was 97.3% of the initial current, which proved that the electrode possessed good stability and reproducibility (Fig. 11).

3.9 Application of colorimetric and electrochemical sensor for real sample analysis

To explore the potential applications of the colorimetric and electrochemical sensor toward DA, standard addition method was applied for serum samples examination. The results were summarized in Table 3. The recoveries were obtained by the standard addition method, and the spiked recoveries were in the range of 96.5%–103.2%, with the relative standard deviations less than 5%. These data indicate that the constructed double-sensor can be successfully applied to simultaneously detecting the levels of DA in real biological samples.

Table 3 The determination results of DA (n = 3) in human serum

Sample	Added (μM)	Found (μM)	Recovery (%)	RSD (%)
Colorimetric				
1	2	1.93	96.5	4.35
2	8	7.86	98.3	3.41
3	12	12.21	101.8	3.67
Electrochemical				
1	5	5.16	103.2	3.46
2	35	35.73	102.1	2.15
3	65	64.56	99.3	1.78

4. Conclusion

In this work, an *in situ* green synthesis method is proposed, and a novel composite produced by MnO_2 nanoparticles and graphene nanosheets (MnO_2@G) is prepared. The colorimetric and electrochemical analysis double-channel methods for the detection of DA are firstly designed based on the excellent oxidase-like activity and electrochemical performance of MnO_2@G. Through comparing the designed two strategy, the colorimetric sensing platform demonstrated lower detection limit with 0.14 μM and higher sensitivity. The electrochemical analysis methods exhibit the advantages of wider linear range with from 0.4 to70 μM and good selectivity. Furthermore, the MnO_2@G nanozyme-based double sensing platform with recoveries from 96.5% to 103.2%, and RSD values were less than 4.35% was used for the successful quantitative testing of DA in clinical serum samples. Therefore, the proposed detection platform provided complementary colorimetric and electrochemical modes to meet the requirements of different occasions. Furthermore, we believe the novel nano-composite MnO_2@G should also possess potential in other applications such as catalyst, absorption, *etc.*, for its unique microstructure.

Conflicts of interest

The authors declare no conflict of interest.

Acknowledgements

The authors acknowledge support from the financial support by the National Natural Science Foundation of China (No. 22066010); the Science and Technology Plan Research Project of Hubei Education Department (Q20211905); Incubation Project for High-Level Scientific Research Achievements of Hubei Minzu University (No. PY22004).

References

1 L. Fan, X. Ji, G. Lin, K. Liu, S. Chen, G. Ma, W. Xue, X. Zhang and L. Wang, *Microchem. J.*, 2021, **166**, 106202.
2 J. Wu, X. Wang, Q. Wang, Z. Lou, S. Li, Y. Zhu, L. Qin and H. Wei, *Chem. Soc. Rev.*, 2019, **48**, 1004–1076.
3 A. Mandal, S. Dasgupta, A. Adhikary, D. Samanta, E. Zangrando and D. Das, *Dalton Trans.*, 2020, **49**, 5999–6011.
4 Q. Li, D. Yu, C. Fan, Q. Huang, Y. Tang, R. Guo, Y. Huang, H. Wang, C. Lin and Y. Lin, *ACS Appl. Nano Mater.*, 2021, **5**, 94–100.
5 L. Liu, C. Wang, Y. Li, L. Qiu, S. Zhou, P. Cui, P. Jiang, X. Ni, R. Liu, X. Du, J. Wang and J. Xia, *Biomater. Sci.*, 2021, **9**, 5965–5976.
6 K. Wei, H. Rao, X. Xue, M. Luo and Z. Xue, *Microchem. J.*, 2021, **170**, 106736.
7 R. Yao, Z. Li, J. Li, K. Tuo, D. Zhang, C. Fan, G. Liu, Y. Deng and S. Pu, *Microchem. J.*, 2023, **193**, 109214.
8 X. Wang, Q. Sun, J. Yu, J. Sun, N. Niu and L. Chen, *Microchem. J.*, 2023, **195**, 109381.
9 D. Zhang, D. Kukkar, H. Kaur and K.-H. Kim, *Adv. Colloid Interface Sci.*, 2023, **319**, 102968.
10 X. Xu, Q. Sun, Y. Ma, X. Jiang, N. Niu and L. Chen, *Sens. Actuators, B*, 2022, **364**, 131881.
11 G. Ren, F. Dong, Z. Zhao, K. Li and Y. Lin, *ACS Appl. Mater. Interfaces*, 2021, **13**, 52987–52997.
12 J. Ge, L. Yang, Z. Li, Y. Wan, D. Mao, R. Deng, Q. Zhou, Y. Yang and W. Tan, *J. Hazard. Mater.*, 2022, **436**, 129199.
13 X. Han, L. Liu, H. Gong, L. Luo, Y. Han, J. Fan, C. Xu, T. Yue, J. Wang and W. Zhang, *Food Chem.*, 2022, **371**, 131115.
14 M. Talebi, K. Dashtian, R. Zare-Dorabei, H. Ghafuri, M. Mahdavi and F. Amourizi, *Anal. Chim. Acta*, 2023, **1247**, 340924.
15 Y. Liu, P. Zhao, Y. Liang, Y. Chen, J. Pu, J. Wu, Y. Yang, Y. Ma, Z. Huang, H. Luo, D. Huo and C. Hou, *Talanta*, 2023, **254**, 124171.
16 N. Alizadeh, S. Ghasemi, A. Salimi, T. K. Sham and R. Hallaj, *Colloids Surf., B*, 2020, **195**, 111228.
17 G. Zhang, L. Zhang, Y. Yu, B. Lin, Y. Wang, M. Guo and Y. Cao, *Biosens. Bioelectron.*, 2020, **167**, 112502.
18 X. Zhang, J. Qiao, W. Liu and L. Qi, *Analyst*, 2021, **146**, 5061–5066.
19 Z. Mu, S. Wu, J. Guo, M. Zhao and Y. Wang, *ACS Sustain. Chem. Eng.*, 2022, **10**, 2984–2993.
20 T. Hallaj, N. Azizi and M. Amjadi, *Microchem. J.*, 2021, **162**, 105865.
21 C. Zhou, J. Chen, G. Wang and X. Su, *Mikrochim. Acta*, 2022, **189**, 135.
22 L. Mei, S. Zhu, Y. Liu, W. Yin, Z. Gu and Y. Zhao, *Chem. Eng. J.*, 2021, **418**, 129431.
23 J. Liu, L. Meng, Z. Fei, P. J. Dyson, X. Jing and X. Liu, *Biosens. Bioelectron.*, 2017, **90**, 69–74.
24 S. Luo, M. Sha, F. Tian, X. Li, L. Fu, Y. Gu, L.-L. Qu, G.-H. Yang and C. Zhu, *Chin. Chem. Lett.*, 2022, **33**, 344–348.
25 L. Gao, J. Zhuang, L. Nie, J. Zhang, Y. Zhang, N. Gu, T. Wang, J. Feng, D. Yang, S. Perrett and X. Yan, *Nat. Nanotechnol.*, 2007, **2**, 577–583.
26 P. Borthakur, P. K. Boruah and M. R. Das, *ACS Sustain. Chem. Eng.*, 2021, **9**, 13245–13255.
27 J. Peng and J. Weng, *Biosens. Bioelectron.*, 2017, **89**, 652–658.
28 S. Dutta, C. Ray, S. Mallick, S. Sarkar, R. Sahoo, Y. Negishi and T. Pal, *J. Phys. Chem. C*, 2015, **119**, 23790–23800.
29 Y. Song, K. Qu, C. Zhao, J. Ren and X. Qu, *Adv. Mater.*, 2010, **22**, 2206–2210.
30 C. Liu, Y. Zhao, D. Xu, X. Zheng and Q. Huang, *Anal. Bioanal. Chem.*, 2021, **413**, 4013–4022.
31 L. Guo, H. Zheng, C. Zhang, L. Qu and L. Yu, *Talanta*, 2020, **210**, 120621.
32 Y. Wang, L. Yang, Y. Liu, Q. Zhao, F. Ding, P. Zou, H. Rao and X. Wang, *Mikrochim. Acta*, 2018, **185**, 496.
33 J. Song, H. Li, H. Shen, X. Zhang, P. Su and Y. Yang, *New J. Chem.*, 2019, **43**, 19053–19062.
34 H.-L. Xu and W.-D. Zhang, *Chin. Chem. Lett.*, 2017, **28**, 143–148.
35 J. Chen, Y. Li, L. Huang, C. Li and G. Shi, *Carbon*, 2015, **81**, 826–834.
36 J. Zhao, Y. Li, Y. He and J. Luo, *ACS Appl. Mater. Interfaces*, 2019, **11**, 36931–36938.
37 W. He, Y. Liu, J. Yuan, J. J. Yin, X. Wu, X. Hu, K. Zhang, J. Liu, C. Chen, Y. Ji and Y. Guo, *Biomaterials*, 2011, **32**, 1139–1147.
38 L. Chen, T. Hou, Y. Tan, C. Guo, B. Wang, L. Ge and F. Li, *ACS Sustain. Chem. Eng.*, 2022, **10**, 2750–2760.
39 T. Barudžija, N. Cvjetićanin, D. Bajuk-Bogdanović, M. Mojović and M. Mitrić, *J. Alloys Compd.*, 2017, **728**, 259–270.
40 T. Gao, M. Glerup, F. Krumeich, R. Nesper, H. Fjellvåg and P. Norby, *J. Phys. Chem. C*, 2008, **112**, 13134–13140.
41 F. Liu, Z. Li, G. Kang, Z. Liu, S. Zhu, R. He, C. Zhang, C. Chen and Y. Lu, *Microchem. J.*, 2023, **186**, 108352.
42 M. X. Liu, H. Zhang, S. Chen, Y. L. Yu and J. H. Wang, *Anal. Bioanal. Chem.*, 2021, **413**, 4451–4458.
43 F.-X. Tian, M. Zhu, X. Liu, W. Tu and Y.-F. Han, *J. Catal.*, 2021, **401**, 115–128.
44 M. H. M. Facure, R. S. Andre, L. A. Mercante and D. S. Correa, *ACS Appl. Nano Mater.*, 2022, **5**, 15211–15219.
45 X. Zhu, J. Xu, X. Duan, L. Lu, K. Zhang, Y. Yu, H. Xing, Y. Gao, L. Dong, H. Sun and T. Yang, *J. Electroanal. Chem.*, 2015, **757**, 183–191.
46 M. C. Liu, L. B. Kong, P. Zhang, Y. C. Luo and L. Kang, *Electrochim. Acta*, 2012, **60**, 443–448.
47 X. Huang and Z. Nan, *Talanta*, 2020, **216**, 120995.
48 Y. Liu, J. Yan, Z. Sun, Y. Huang, X. Li and Y. Jin, *Mikrochim. Acta*, 2022, **189**, 63.
49 J. Liu, L. Meng, Z. Fei, P. J. Dyson and L. Zhang, *Biosens. Bioelectron.*, 2018, **121**, 159–165.
50 X. Dan, L. Ruiyi, W. Qinsheng, Y. Yongqiang, W. Guangli and L. Zaijun, *Microchem. J.*, 2021, **166**, 106204.
51 M. Cui, J. Zhou, Y. Zhao and Q. Song, *Sens. Actuators, B*, 2017, **243**, 203–210.
52 Y. Liu, M. Zhou, W. Cao, X. Wang, Q. Wang, S. Li and H. Wei, *Anal. Chem.*, 2019, **91**, 8170–8175.
53 X. Yan, Y. Gu, C. Li, L. Tang, B. Zheng, Y. Li, Z. Zhang and M. Yang, *Biosens. Bioelectron.*, 2016, **77**, 1032–1038.

54 Y. Li, Y. Gu, B. Zheng, L. Luo, C. Li, X. Yan, T. Zhang, N. Lu and Z. Zhang, *Talanta*, 2017, **162**, 80–89.
55 N. Lu, X. Yan, Y. Gu, T. Zhang, Y. Liu, Y. Song, Z. Xu, Y. Xing, X. Li, Z. Zhang and S. Zhai, *Electrochim. Acta*, 2021, **395**, 139197.
56 H. Liu, C. Liu, Y. Gu, C. Li, X. Yan, T. Zhang, N. Lu, B. Zheng, Y. Li, Z. Zhang and M. Yang, *Biosens. Bioelectron.*, 2018, **99**, 296–302.
57 J. Zhu, X. Peng, W. Nie, Y. Wang, J. Gao, W. Wen, J. N. Selvaraj, X. Zhang and S. Wang, *Biosens. Bioelectron.*, 2019, **141**, 111450.
58 M. N. Ivanova, E. D. Grayfer, E. E. Plotnikova, L. S. Kibis, G. Darabdhara, P. K. Boruah, M. R. Das and V. E. Fedorov, *ACS Appl. Mater. Interfaces*, 2019, **11**, 22102–22112.
59 Y.-S. Hsieh, B.-D. Hong and C.-L. Lee, *Microchim. Acta*, 2015, **183**, 905–910.
60 I. Anshori, K. A. A. Kepakisan, L. Nuraviana Rizalputri, R. Rona Althof, A. E. Nugroho, R. Siburian and M. Handayani, *Nanocomposites*, 2022, **8**, 155–166.
61 D. E. Oh, C. S. Lee and T. H. Kim, *Talanta*, 2022, **247**, 123590.